Journal of Computational Physics 228 (2009) 2918–2933

Contents lists available at ScienceDirect

Journal of Computational Physics

journal homepage: www.elsevier.com/locate/jcp

The influence of cell geometry on the accuracy of upwind schemes in the low mach number regime

Felix Rieper [a,*], Georg Bader [b]

[a] Institut für Atmosphäre und Umwelt, Goethe-Universität Frankfurt, Altenhöferallee 1, D-60438 Frankfurt am Main, Germany
[b] Institute for Applied Mathematics and Scientific Computing, Brandenburgische Technische Universtität Cottbus, Konrad-Wachsmann-Allee 1, D-03046 Cottbus

ARTICLE INFO

Article history:
Received 8 May 2008
Received in revised form 11 December 2008
Accepted 5 January 2009
Available online 16 January 2009

PACS:
47.11.Df
47.11.–j
47.15.G–
47.15.km

Keywords:
Incompressible and compressible flow
Euler equations
Low Mach number flow
Roe scheme
Numerical dissipation
Asymptotic analysis

ABSTRACT

It is well known, that standard upwind schemes for the Euler equations face a number of problems in the low Mach number regime: stiffness, cancellation and accuracy problems. A new aspect, presented in this paper, is the dependence on the cell geometry: applied on a triangular grid, the accuracy problem disappears, i.e. flows of arbitrarily small Mach numbers can be simulated on a fixed mesh. We give an asymptotic analysis of this, up to date unknown, phenomenon for the first-order Roe scheme and present a number of numerical results.

1. Introduction

Schemes, originally designed to calculate compressible flow, encounter three problems in low Mach number flow:

(1) The wave speeds of acoustic and flow phenomena are of different orders of magnitude – their ratio is measured by the Mach number. Low Mach numbers slow down the calculation of phenomena on the time scale of the flow such as heat or water transport (*stiffness problem*).
(2) The pressure variable has to accommodate a constant background pressure of order $\mathcal{O}(1)$ and the physically relevant pressure variations of order $\mathcal{O}(M^2)$, which leads to numerical round-off errors (*cancellation problem*).
(3) For stability reasons, upwind schemes introduce artificial viscosity, which depends on the Mach number. In certain settings this can cause the truncation error to grow with decreasing Mach numbers (on a fixed mesh), preventing the numerical solution to approximate inviscid, incompressible flow (*accuracy problem*).

* Corresponding author. Tel.: +49 (0) 69 798 40241.
E-mail addresses: rieper@iau.uni-frankfurt.de (F. Rieper), bader@math.tu-cottbus.de (G. Bader).

0021-9991/$ - see front matter © 2009 Elsevier Inc. All rights reserved.
doi:10.1016/j.jcp.2009.01.002

The *cancellation problem* can be avoided by working only with the fluctuation quantities introduced in the wave propagation approach by Leveque [1]. This approach was applied to low Mach number flow by Sesterhenn et al. [2]. To overcome the *stiffness problem in steady flow simulations*, a variety of time-derivative or flux preconditioning techniques have been developed and applied to compressible (and incompressible) solvers for the inviscid flow equations, such as Turkel's approach, [3,4], or the characteristic time stepping approach by van Leer et al. [5]. The stiffness is reduced by (almost) equalising the propagation speeds of the different waves for $M \to 0$, which accelerates the convergence to steady state. At the same time, the artificial viscosity is tuned correctly for all characteristic waves and thus the accuracy problem is circumvented. Preconditioning in the context of viscous flow was dealt with by Choi and Merkle in [6]. In addition, the authors report on the absence of the accuracy problem down to $M = 10^{-6}$ for their preconditioning methods, which are implemented on grids with quadrilateral cells. The *accuracy problem* was explicitly addressed and solved with a preconditioning of the numerical dissipation tensor by Guillard and Viozat [7]. Their asymptotic analysis of the Roe scheme illuminates the reason for its failure for $M \to 0$ on *Cartesian grids*.

2. Numerical experiments

In this section we present a variety of numerical experiments with the explicit, *non-preconditioned*, first-order Roe scheme that all suggest an intriguing result: the accuracy depends on the geometry of the finite volume cell. On *Cartesian grids* the accuracy of the results deteriorates with decreasing Mach numbers, while the accuracy is maintained on *triangular grids*.

2.1. Flow around a cylinder

The flow around a cylinder is very useful since we know the incompressible potential flow solution, i.e. we have an analytical reference solution for $M \to 0$. The *initial conditions* are set uniform to $\rho_0 = 1.0, \mathbf{u}_0 = (u_0, 0)^T, p_0 = 1.0$, where the absolute value $\|\mathbf{u}_0\| = \sqrt{\gamma} M_0$ of the initial velocity is set to meet the prescribed initial Mach number M_0, and γ is the adiabatic index set to 1.4 throughout our calculations. The exact solution at infinity is assumed uniform

$$\rho_\infty = 1.0, \quad \mathbf{u}_\infty = (u_\infty, 0)^T, \quad p_\infty = 1.0.$$

In the *far-field boundary conditions* this solution is assumed to be a good approximation of the solution at the outer boundary. These values are prescribed in the ghost cells.

For the body-fitted, structured grid we use a division into $n_\phi = 150$ cells along the circumference and $n_r = 50$ along the radius. We start the calculations on a regular cylinder grid, also called polar grid, and continuously transform it to a triangular grid. This transition is implemented by reducing the original length Δx_0 of one of the four edges of the quasi square cell by a factor 10^n. The resulting edge has length $\Delta x = \Delta x_0 / 10^n$ and belongs to a trapezoid, which converges for $n \to \infty$ to a triangular cell. In the finite volume context the flux across the 'squeezed' edge also converges to zero. In Fig. 1 cells of the grid and, underneath, the corresponding isolines of pressure are shown. On the regular grid (left) the solution is completely wrong. The trapezoidal cells in the middle lead to a solution that is 'on the right way'. The isolines of pressure in the right figure are of good accuracy. Further reduction of Δx does not improve the accuracy – the ratio $\Delta x / \Delta x_0$ has reached a critical value. The question is, does the critical ratio depend on the inflow Mach number?

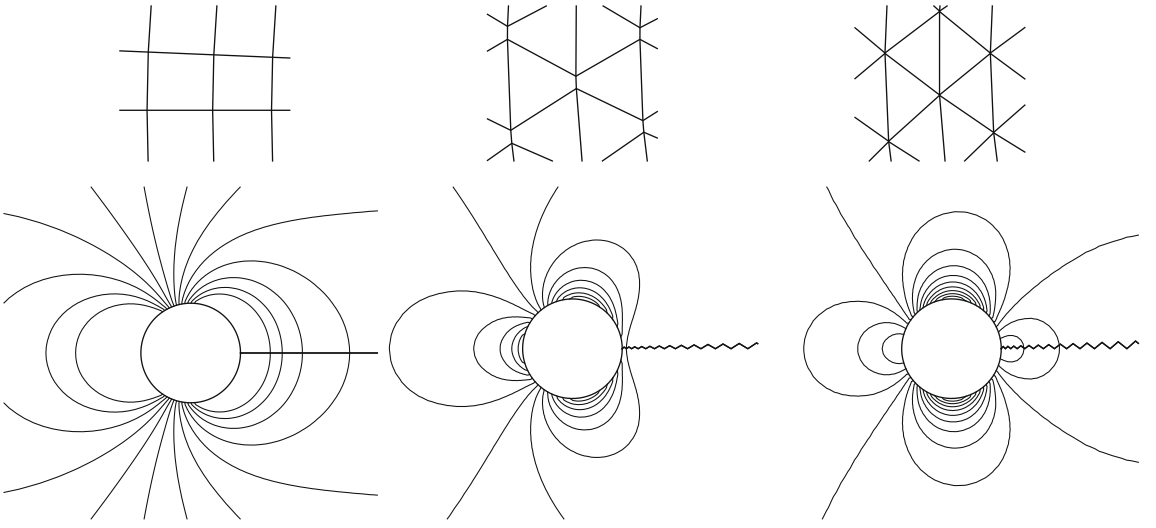

Fig. 1. Flow around a cylinder with the classical first-order Roe scheme on a grid with 150×50 cells at $M_0 = 10^{-2}$. Top line: trapezoidal cells converging to triangular cells. Bottom line: corresponding isolines of pressure.

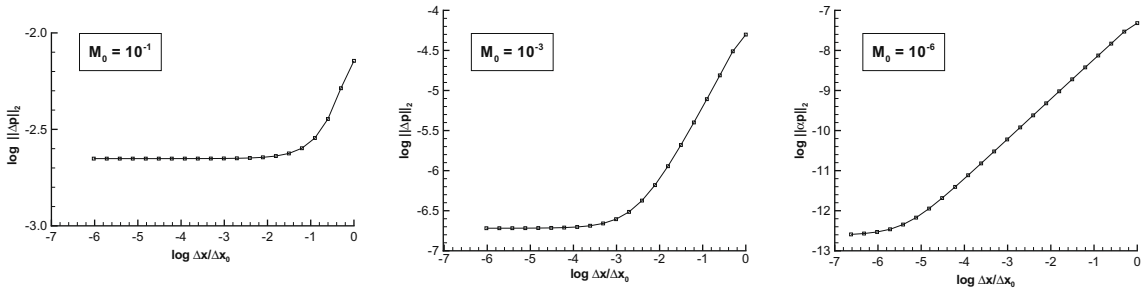

Fig. 2. L_2-error of the pressure as a function of grid cell shape: $\Delta x = \Delta x_0$ represents regular grid cells and $\Delta x/\Delta x_0 \approx 0$ approximately triangular grid cells.

In Fig. 2 we show the results of a study to clear this question. It can be seen, how the accuracy improves, when the cell shape approaches a triangle. The abscissa shows the ratio of original edge length Δx_0 to the reduced edge length Δx on a logarithmic scale: $\log \Delta x/\Delta x_0$. The ordinate represents the L_2 pressure deviation from the incompressible potential flow solution on a logarithmic scale. Comparing the diagrams, we see that for $M_0 = 10^{-k}$ the L_2-error of the pressure reaches a plateau once the edge length Δx is reduced by a factor of about 10^k.

Structured vs. unstructured triangular grids. The previous experiment on *structured grids* leaves an open question: is the *accuracy problem* present on unstructured triangular grids? To find an answer we repeated the simulation on an unstructured cylinder grid with approximately the same resolution. The results, cf. [8], are of comparable accuracy.

Note on unstructured quadrilateral grids. A similar experiment was done with an unstructured grid of quadrilateral finite volume cells. The deviation of the regular grid was obtained with a random shift of the grid vertices. The isolines of pressure, compared to the regular grid, did not improve. We therefore conclude, that the reason for the *accuracy problem* is not linked to the grid structure as a whole, but to the geometry of the finite volume cell.

2.2. Flow around a square

The flow around a square has a major advantage: we can work on a Cartesian grid, which simplifies the analysis. We compare the solution obtained on a Cartesian grid with the one obtained on a related triangulation as depicted in Fig. 3. Note that the diagonals are introduced in a uniform direction from the lower left to the upper right corner of the Cartesian cells.

The resulting grids for the flow around a square are depicted on the left column of Fig. 4. To make the calculations on the quadratic flow domain comparable, the total number of cells were chosen to be similar: $2 \times 35 \times 35 = 2450$ in the triangulation and 50×50 in the Cartesian mesh – minus the cells covered by the rectangular obstacle. The initial and boundary conditions are set analogously to the ones for the flow around a cylinder. The angle of attack was set to $\alpha = 45^\circ$. Note that an inflow "against" the diagonals does not significantly change the result.

On the right of Fig. 4 the isolines of pressure for an inflow Mach number of $M_0 = 10^{-3}$ and an angle of attack of $\alpha = 45^\circ$ are shown. For this test case we do not know the exact solution, yet, we expect the maximum pressure in the stagnation point to be about $\frac{1}{2}\gamma M_0^2$ (Bernoulli's principle). This is well approximated on the triangular grid and overestimated by a factor of 100 on the Cartesian grid, where, in addition, the isolines of pressure are grid-aligned.

2.3. A steady shear layer

We suggest an even simpler test case: the inflow of a contact discontinuity. Investigated are two types: a steady *entropy layer* and a steady *shear layer*, which are set up oblique to the grid lines by the inflow boundary conditions. The same grids are used as for the Gresho vortex simulation.

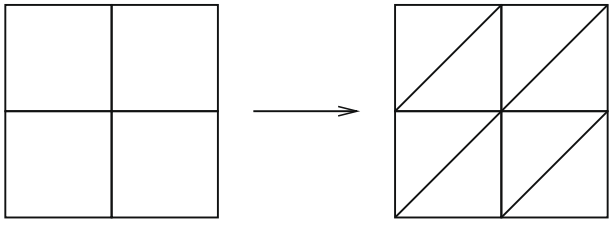

Fig. 3. Creating a triangular grid from a Cartesian grid.

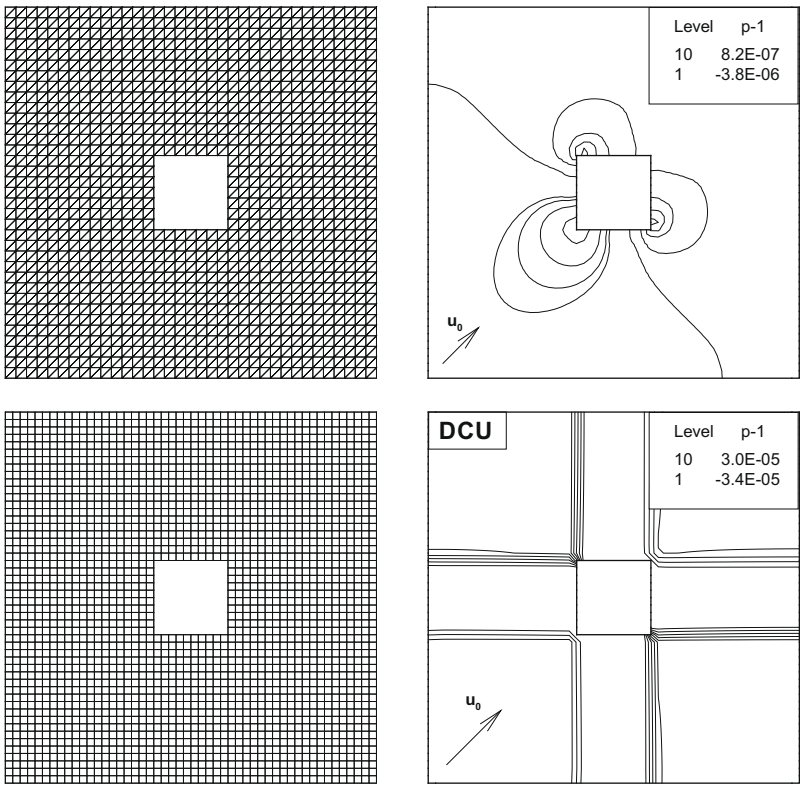

Fig. 4. Isolines of pressure for the flow around a square at $M = 10^{-3}$.

It can be observed – for both types of grid – that the smearing of an inflowing *entropy contact* depends on the angle, but there is no dependency on the Mach number, cf. [8]. The situation is entirely different for shear layers. We therefore only present the more interesting results for a *shear flow*. The settings are: on the left and bottom edge of the rectangular flow domain $\Omega = [0,1] \times [0,1]$ we choose *inflow boundary conditions* with constant density $\rho_{\text{ghost}} = 1.0$ and a jump in the prescribed inflow velocity:

$$\mathbf{u}_{\text{ghost}} = \begin{cases} 1.0\|\mathbf{u}_{\text{in}}\|(\cos\alpha, \sin\alpha)^T & y \leqslant 0.5, \\ 1.1\|\mathbf{u}_{\text{in}}\|(\cos\alpha, \sin\alpha)^T & y > 0.5, \end{cases}$$

where $\alpha = 10^\circ$ is the angle of inflow in this test case. The absolute value $\|\mathbf{u}_{\text{in}}\| = \sqrt{\gamma}M_0$ is tuned to meet the prescribed Mach number M_0. The pressure in the ghost cells p_{ghost} next to the inflow boundary is extrapolated from the neighbouring interior cells. For the right and upper boundary we impose *outflow boundary conditions* by extrapolating the values of density, velocity and pressure into the ghost cells.

In Fig. 5, on the left columns, we see the isolines of the Mach number obtained on a grid with $2 \times 50 \times 50$ triangular finite volume cells and on the right column the results for a Cartesian grid with 70×70 cells. In the background the grid lines are indicated in a light grey. We make two major observations: on *triangular finite volume cells* the numerical dissipation is independent of the Mach number and the angle of the shear layer agrees with the inflow boundary condition. On *Cartesian cells* the shear layer is bent towards the grid lines for decreasing Mach numbers until it is, for $M_0 \approx 10^{-3}$, completely aligned to the grid.

2.4. Proposal

All simulations suggest that the accuracy problem occurs on *Cartesian grids* and manifests itself in a Mach number dependent dissipation of flow structures. The accuracy seems to be independent of the Mach number if the *first-order* Roe method is used on *triangular finite volume cells*. This will be analysed in detail in the following.

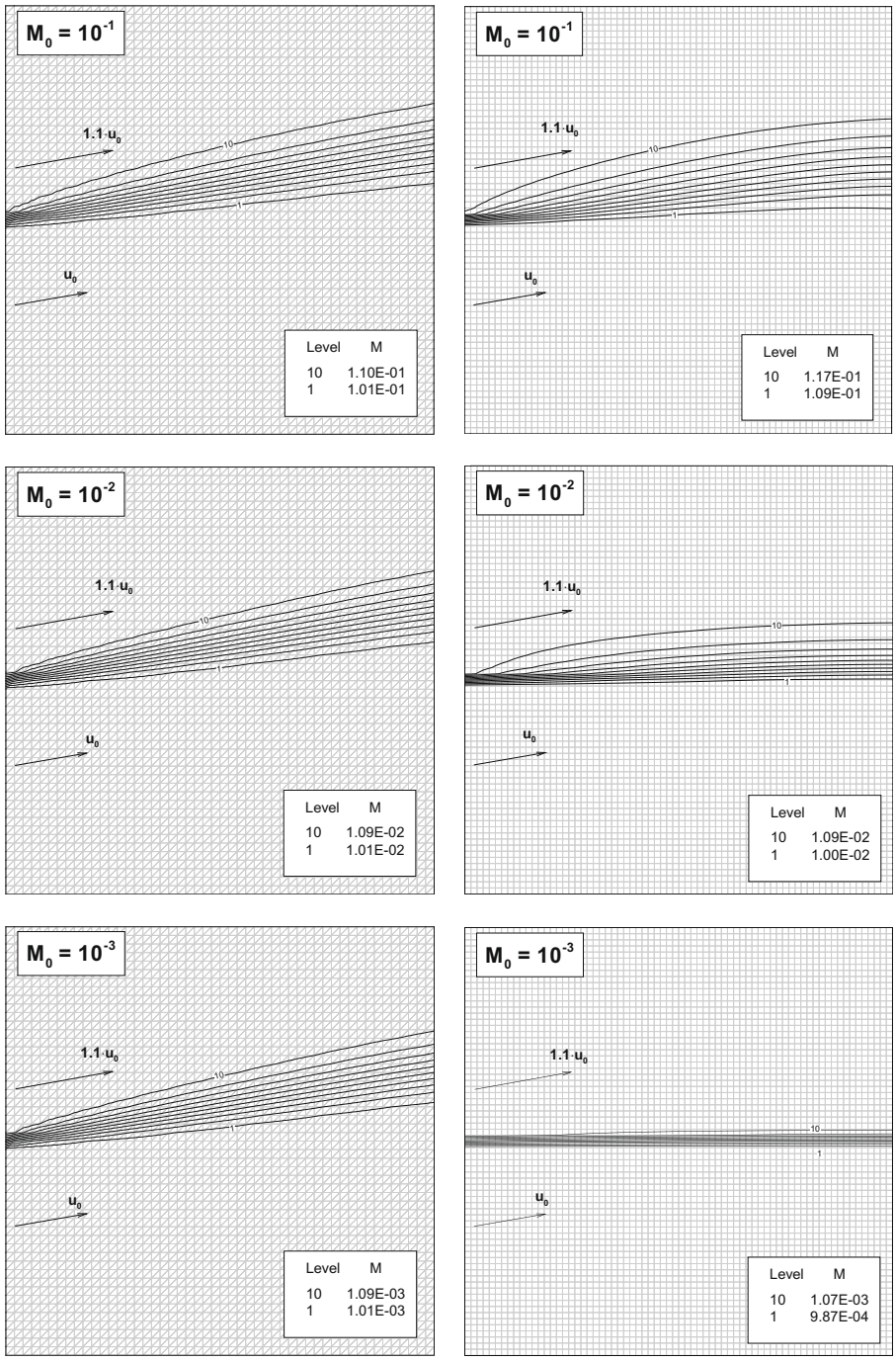

Fig. 5. Inflow of a shear discontinuity on a grid with $2 \times 50 \times 50$ triangular cells (left column) and 70×70 square cells (right column). The inflow angle is set to $\alpha = 10^{\circ}$ and the inflow velocity is set according to the given Mach number ranging from $M_0 = 10^{-1}$ down to $M_0 = 10^{-3}$. In the upper half of the grid the inflow Mach number is 1.1 times larger than in the lower half.

3. Asymptotic analysis

3.1. Introduction

The 2D Euler equations can be written as:

$$\frac{\partial \mathbf{q}}{\partial t} + \nabla \cdot F(\mathbf{q}) = 0, \tag{3.1}$$

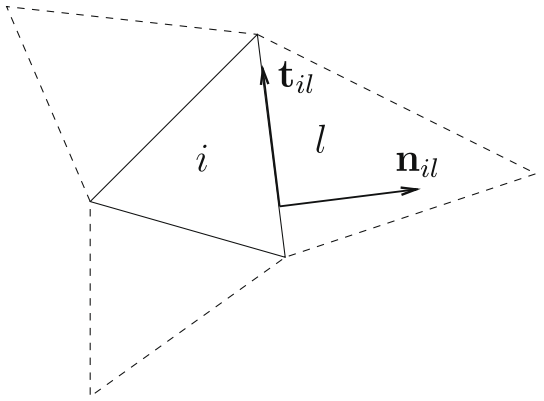

Fig. 6. Index notation and local coordinate system for a triangular grid.

$$F(\mathbf{q}) = \begin{pmatrix} \mathbf{f}(\mathbf{q}) \\ \mathbf{g}(\mathbf{q}) \end{pmatrix}, \tag{3.2}$$

where

$$\mathbf{q} = \begin{bmatrix} \rho \\ \rho u \\ \rho v \\ \rho e \end{bmatrix}, \quad \mathbf{f}(\mathbf{q}) = \begin{bmatrix} \rho u \\ \rho u^2 + p \\ \rho uv \\ (\rho e + p)u \end{bmatrix}, \quad \mathbf{g}(\mathbf{q}) = \begin{bmatrix} \rho v \\ \rho uv \\ \rho v^2 + p \\ (\rho e + p)v \end{bmatrix}. \tag{3.3}$$

Non-dimensionalisation with separate references for flow and sound velocity introduces a $1/\mathrm{M}^2$-factor for the pressure gradient. To analyse the asymptotic behaviour of the equations for $\mathrm{M} \to 0$, it is customary to assume an asymptotic 3-term expansion of the physical quantities in terms of the small Mach number

$$\phi = \phi^{(0)} + \mathrm{M}\phi^{(1)} + \mathrm{M}^2\phi^{(2)} + \mathcal{O}(\mathrm{M}^2) \quad \text{as } \mathrm{M} \to 0,$$

where ϕ can either be velocity $\mathbf{u}$, pressure p or density ρ. Note that in steady low Mach number flow, the Euler equations are characterised by a constant background pressure $p^{(0)}$ and variations in $p^{(2)}$, cf. [9]. It is worth mentioning, that in unsteady flow $p^{(1)}$ can be present: for example a global compression $\nabla \cdot \mathbf{u}^{(0)} < 0$ leads to pressure perturbations in $p^{(1)}$ on the acoustic time scale (and a pressure increase in $p^{(0)}$ on the time scale of the flow), cf. [8].

A rigorous asymptotic analysis of the semi-discrete Roe scheme on *Cartesian grids* was given by Guillard and Viozat in [7]. They show the existence of an unphysical pressure variation in $p^{(1)}$. A plausible explanation of this phenomenon is also given in [8]. The numerical behaviour of the Roe scheme on *triangular grids* is entirely different: there is no variation in $p^{(1)}$, as will be shown next. This physically correct behaviour is accompanied by a constraint: $\Delta U^{(0)} = 0$, i.e. the leading-order velocity component normal to a cell edge does not jump. In the last section we show that this constraint leaves enough degrees of freedom for the velocity field to represent a physical flow.

For simplicity, the analysis is restricted to triangular finite volume cells derived from Cartesian grid cells by introducing a diagonal as an additional cell edge dividing the square into a *upper* and a *lower* triangle, see Fig. 7. We further restrict the analysis to steady flow with a constant background density $\rho^{(0)} = \text{const}$. The asymptotic equations of the semi-discrete Roe scheme are derived in the Appendix and are written with the notation similar to [7] with indices as depicted in Fig. 6: cell indices are i or j and $v(i)$ is the set of neighbouring cells. The area of the reference cell is A_i. Symbol il denotes the edge between cell i and l with length δ_{il} and $\mathbf{n}_{il}$ the corresponding outer normal vector. The difference is given by

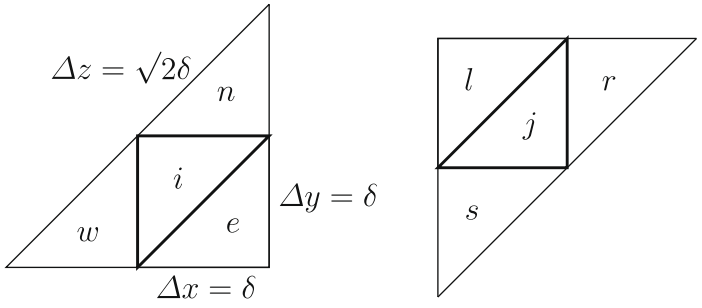

Fig. 7. Indices for upper triangle (left) and lower triangle (right).

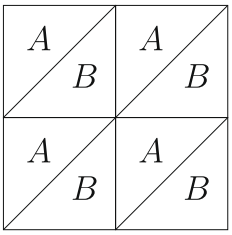

Fig. 8. Two-value structure of the leading-order pressure $p^{(0)}$.

$\Delta_{il}\phi = \phi_i - \phi_l$, and ϕ_{il} is the Roe average of ϕ_i and ϕ_l. The normal component of $\mathbf{u}$ is $U = \mathbf{u}\cdot\mathbf{n}$ and $V = \mathbf{u}\cdot\mathbf{t}$ is the transverse component.

3.2. The leading-order pressure $p^{(0)}$

As a preliminary, we show the uniformity of $p^{(0)}$ – a result which is also valid for Cartesian grids, cf. [7]. The momentum Eqs. (M_x^{-1}) and (M_y^{-1}) corresponding to the $\mathcal{O}_\mathrm{S}(\mathrm{M}^{-1})$ terms, as derived in the Appendix, are

$$\sum_{l\in\nu(j)} p_l^{(0)}\cdot(n_x)_{jl}\delta_{jl} = 0,$$
$$\sum_{l\in\nu(j)} p_l^{(0)}\cdot(n_y)_{jl}\delta_{jl} = 0.$$

They indicate that the central differences of $p^{(0)}$ in horizontal and in vertical direction vanish separately. Applying the simple geometry, cf. right of Fig. 7, we obtain $p_r^{(0)} = p_l^{(0)}$ and $p_l^{(0)} = p_s^{(0)}$ for the lower triangle. An analogous result is true for the upper triangles. These relations restrict $p^{(0)}$ to form a two-value structure as depicted in Fig. 8. To show uniformity of $p^{(0)}$, we use the steady form of the evolution equation of $p^{(0)}$ as derived in the Appendix:

$$\frac{\gamma-1}{2}\frac{1}{A_i}\sum_{l\in\nu(j)}\frac{h_{jl}^{(0)}}{a_{jl}^{(0)}}\Delta_{jl}p^{(0)}\delta_{jl} = 0. \tag{P_0}$$

Let us assume, without loss of generality, that $p_j^{(0)} = A > B$. Then all pressure differences in (P_0) satisfy

$$\Delta_{jl}p^{(0)} = A - B > 0,$$

so that the sum in (P_0) has to be greater than zero, which contradicts the equality to zero. Therefore $A = B$ and the pressure of leading order has to be constant:

$$\boxed{p_i^{(0)} = p_j^{(0)} \quad \text{for } i,j\in\Omega.}$$

The constant background pressure $p^{(0)}$ is specified by the boundary conditions.

3.3. The first-order pressure $p^{(1)}$

To show the constancy of the first-order pressure $p^{(1)}$ we analyse the equations for the leading order velocity in horizontal and vertical direction, $u^{(0)}$ and $v^{(0)}$, as well as the equation for the first-order pressure $p^{(1)}$. In the following analysis let us introduce reference quantities, such that

$$p^{(0)} = \frac{1}{\sqrt{\gamma}}, \quad \rho^{(0)} = 1 \Rightarrow [a^{(0)}]^2 = \frac{\gamma p^{(0)}}{\rho^{(0)}} = 1. \tag{3.4}$$

This is possible since $p^{(0)} = \text{const}$. The assumption $\rho^{(0)} = \text{const}$ is sensible as we have seen in Section 2 that density jumps are transported independently of the Mach number. To facilitate reading, we omit the superscripts and identify $p^{(1)} \rightsquigarrow p$, $U^{(0)} \rightsquigarrow U$ whenever there is no risk of confusing different order terms. Note that for *upper* and *lower triangle* different sets of indices are used. The edge lengths $\Delta x = \Delta y = \delta$ drop out of the equations and all time derivatives are omitted because we analyse the steady case.

The equation for $u^{(0)}$ as derived in Appendix A.1.2 is

$$\underbrace{\frac{\mathrm{d}}{\mathrm{d}t}u_i^{(0)}}_{\frac{\partial}{\partial t}u^{(0)}} + \underbrace{\frac{1}{\rho_i^{(0)}}\frac{1}{A_i}\sum_{l\in\nu(i)}\frac{p_l^{(1)}(n_x)_{il}}{2}\delta_{il}}_{\frac{1}{\rho^{(0)}}\frac{\partial}{\partial x}p^{(1)}} = \underbrace{-\frac{1}{2}\frac{a_i^{(0)}}{\rho_i^{(0)}}\frac{1}{A_i}\sum_{l\in\nu(i)}\rho_{il}^{(0)}\Delta_{il}U^{(0)}(n_x)_{il}\delta_{il}}_{\frac{1}{2}a^{(0)}\frac{1}{2}\frac{\partial^2}{\partial x^2}u^{(0)}\delta}, \tag{U_0}$$

where the underbracing shows the continuous counterparts. With the assumptions (3.4) and the simple geometry, Eq. (U_0) can be written for the *upper triangle* as

$$p_e\delta - p_w\delta + \Delta_{ie}U\delta - \Delta_{iw}U\delta = 0.$$

If we add $(-p_i + p_i)\delta$ to the LHS, the pressure variables can be transformed into jump variables:

$$\boxed{\Delta_{iw}p - \Delta_{ie}p + \Delta_{ie}U - \Delta_{iw}U = 0.} \tag{3.5}$$

The analogous equation for the *lower triangle* is

$$\boxed{\Delta_{jl}p - \Delta_{jr}p + \Delta_{jr}U - \Delta_{jl}U = 0.} \tag{3.6}$$

The equation for $v^{(0)}$ as derived in Appendix A.1.2 reads

$$\underbrace{\frac{\mathrm{d}}{\mathrm{d}t}v_i^{(0)}}_{\frac{\partial}{\partial t}v^{(0)}} + \underbrace{\frac{1}{\rho_i^{(0)}}\frac{1}{A_i}\sum_{l\in v(i)}\frac{p_l^{(1)}(n_y)_{il}}{2}\delta_{il}}_{\frac{1}{\rho^{(0)}}\frac{\partial}{\partial y}p^{(1)}} = -\underbrace{\frac{1}{2}\frac{a_i^{(0)}}{\rho_i^{(0)}}\frac{1}{A_i}\sum_{l\in v(i)}\rho_{il}^{(0)}\Delta_{il}U^{(0)}(n_y)_{il}\delta_{il}}_{\frac{1}{2}a^{(0)}\frac{\partial^2}{\partial y^2}v^{(0)}\delta}. \tag{V^0}$$

This equation can be transformed in a similar way for the *upper triangle* to

$$\boxed{\Delta_{ie}p - \Delta_{in}p - \Delta_{ie}U + \Delta_{in}U = 0,} \tag{3.7}$$

and for the lower triangle to

$$\boxed{\Delta_{js}p - \Delta_{jl}p - \Delta_{js}U + \Delta_{jl}U = 0.} \tag{3.8}$$

The equation for $p^{(1)}$, Appendix A.1.2, is given by

$$\underbrace{\frac{\mathrm{d}}{\mathrm{d}t}p_i^{(1)}}_{\frac{\partial}{\partial t}p^{(1)}} + \underbrace{\gamma p_i^{(0)}\frac{1}{A_i}\sum_{l\in v(i)}\frac{\mathbf{u}_l^{(0)}\cdot\mathbf{n}_{il}}{2}\delta_{il}}_{\gamma p^{(0)}\nabla\cdot\mathbf{u}^{(0)}} = -\underbrace{\frac{1}{2}a_i^{(0)}\frac{1}{A_i}\sum_{l\in v(i)}\Delta_{il}p^{(1)}\delta_{il}}_{\frac{1}{2}a^{(0)}\nabla^2 p^{(1)}\delta}. \tag{P^1}$$

We make use of the fact that a closed chain of vectors gives the zero vector, to replace the velocity $\mathbf{u}^{(0)}$ by its corresponding jump variable ΔU:

$$\sum_{l\in v(i)}\mathbf{u}_l^{(0)}\cdot\mathbf{n}_{il}\delta_{il} = \sum_{l\in v(i)}(\mathbf{u}_l^{(0)} - \mathbf{u}_i^{(0)})\cdot\mathbf{n}_{il}\delta_{il} = -\sum_{l\in v(i)}\Delta_{il}U\delta_{il}.$$

We furthermore divide Eq. (P$_1$) by $a_i^{(0)}$ and make use of $\frac{\gamma p^{(0)}}{a^{(0)}} = \rho^{(0)}a^{(0)} = 1$. The pressure equation can then be written as

$$\sum_{l\in v(i)}(\Delta_{il}p - \Delta_{il}U)\delta_{il} = 0. \tag{P^1}$$

If we apply the special geometry of the *upper triangle* to this equation, we obtain

$$\boxed{\sqrt{2}\Delta_{ie}p + \Delta_{in}p + \Delta_{iw}p - \sqrt{2}\Delta_{ie}U - \Delta_{in}U - \Delta_{iw}U = 0.} \tag{3.9}$$

The analogous equation for the *lower triangle* reads redefinitions

$$\boxed{\sqrt{2}\Delta_{jl}p + \Delta_{js}p + \Delta_{jr}p - \sqrt{2}\Delta_{jl}U - \Delta_{js}U - \Delta_{jr}U = 0.} \tag{3.10}$$

The overall system of linear equations consists of three equations per triangle, or six equations per Cartesian cell. To see the relation between these equations, we introduce unified indices for the cell edges as depicted in Fig. 9, along with unified orientations of the local coordinate systems. With the new indices the system of linear Eqs. (3.5)–(3.10) becomes

$$\Delta_2 p + \Delta_3 p + \Delta_3 U - \Delta_2 U = 0, \tag{Ua}$$

$$-\Delta_3 p + \Delta_1 p - \Delta_3 U + \Delta_1 U = 0, \tag{Va}$$

$$-\sqrt{2}\Delta_3 p - \Delta_1 p + \Delta_2 p - \sqrt{2}\Delta_3 U - \Delta_1 U - \Delta_2 U = 0 \tag{Pa}$$

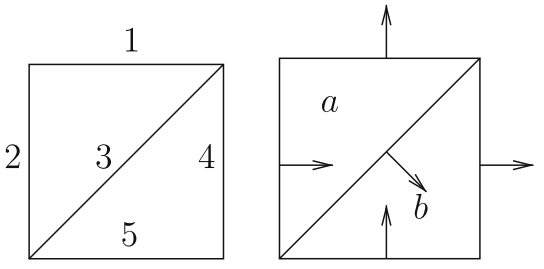

Fig. 9. Unified edge indices (left) and orientation of the local coordinate systems (right) for the upper triangle a and lower triangle b.

for the *upper* triangle and

$$\Delta_3 p + \Delta_4 p + \Delta_4 U - \Delta_3 U = 0, \tag{Ub}$$

$$\Delta_5 p - \Delta_3 p - \Delta_5 U + \Delta_3 U = 0, \tag{Vb}$$

$$\sqrt{2}\Delta_3 p + \Delta_5 p - \Delta_4 p - \sqrt{2}\Delta_3 U - \Delta_5 U - \Delta_4 U = 0 \tag{Pb}$$

for the *lower* triangle. An equivalent system can be derived to be:

$$\Delta_1 p + \Delta_1 U = 0, \tag{3.11a}$$
$$\Delta_5 p - \Delta_5 U = 0, \tag{3.11b}$$
$$\Delta_3 p = 0, \tag{3.11c}$$
$$\Delta_3 U = 0, \tag{3.11d}$$
$$\Delta_4 p + \Delta_4 U = 0, \tag{3.11e}$$
$$\Delta_2 p - \Delta_2 U = 0. \tag{3.11f}$$

This system is valid for each pair of triangles inside a Cartesian cell. From Eqs. (3.11c) and (3.11d) follows that the pressure of first order $p^{(1)}$ and the normal velocity of leading order $U^{(0)}$ do not jump at any *diagonal edge* inside the grid. For **internal edges** let us consider two neighbouring triangle pairs A and B, as depicted in Fig. 10, with a common edge i. The corresponding *two systems* of linear equations have only the jump variables $\Delta_i p$ and $\Delta_i U$ in common. The equation related to i as the right edge is (3.11e), and for i as the left edge is (3.11f), leading to

$$\Delta_i p + \Delta_i U = 0 \quad (\text{right edge}), \tag{3.12}$$
$$\Delta_i p - \Delta_i U = 0 \quad (\text{left edge}) \tag{3.13}$$

with the unique trivial solution: $\Delta_i p = \Delta_i U = 0$. The same can be shown for vertical edges. The unique solution indicates that the jumps of $p^{(1)}$ and $U^{(0)}$ at all internal edges vanish:

$$\boxed{\Delta_i p = 0, \quad \Delta_i U = 0 \text{ for } \quad i \in \Omega/\partial\Omega.} \tag{3.14}$$

This shows that the pressure of first order $p^{(1)}$ is constant *inside the grid*. For a detailed analysis of boundary conditions cf. [8]. In addition, the leading-order velocity $\mathbf{u}^{(0)}$ is *zero-jump constrained*, i.e. the normal component of the velocity field does not jump at cell interfaces.

3.4. Degrees of freedom for $\mathbf{u}^{(0)}$

The question arises, how many degrees of freedom f remain for the velocity field under the zero-jump constraint (3.14). In the following analysis we need concepts, which slightly deviate from standard terms used in graph theory, cf. [10]. We therefore give the following definitions:

Definition 1. The primary grid of finite volume cells induces a *primary grid graph* G or simply primary graph in a straightforward manner: grid edges are edges of the graph and where edges meet, we define the vertices of G.

Definition 2. The *extended dual grid graph* G^* consists of *internal vertices* placed inside each finite volume cell. The ghost cells for boundary conditions give rise to *external vertices*. Two vertices are *neighbours* if the corresponding primary grid cells have a common edge. External vertices are only connected to their internal neighbour vertices – the corresponding edges are called *external edges*. *Internal edges* are the edges connecting internal neighbour vertices with each other.

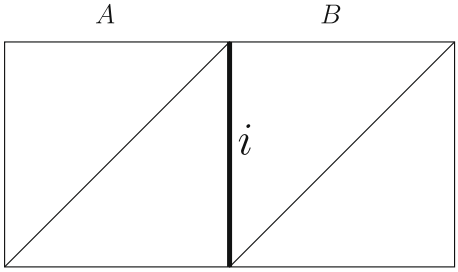

Fig. 10. Neighbouring cells with common edge i.

Recall that a *dual grid graph*, different to its *extended* counterpart defined above, has only one vertex outside the primary grid graph, which corresponds to the face associated with the outer region. Note that in our context of two-dimensional finite volume grids, the corresponding grid graphs and its extended duals are always *finite, connected and planar*.

3.4.1. Motivating example

Before elaborating a rigorous derivation for the degrees of freedom, we give a few motivating examples. For a triangulation derived from a Cartesian grid of size $m \times n$ we ask for the degrees of freedom $f_{m,n}$. Using the example of a grid of size 3×4, we show the general approach to the problem with concepts from graph theory. In Fig. 11(a)–(h) we illustrate how the construction of the extended dual grid graph G^* can be associated with the degrees of freedom. With the thin lines we represent G. The edges of G^* are the thick lines. They represent the 'inheritance' of a velocity component from a neighbouring cell due to the fact, that there are no jumps of the normal velocity component at a cell edge. We emphasise the direction of inheritance in each step by an arrow head. The sequence of construction is indicated in each subfigure by numbers next to a new edge.

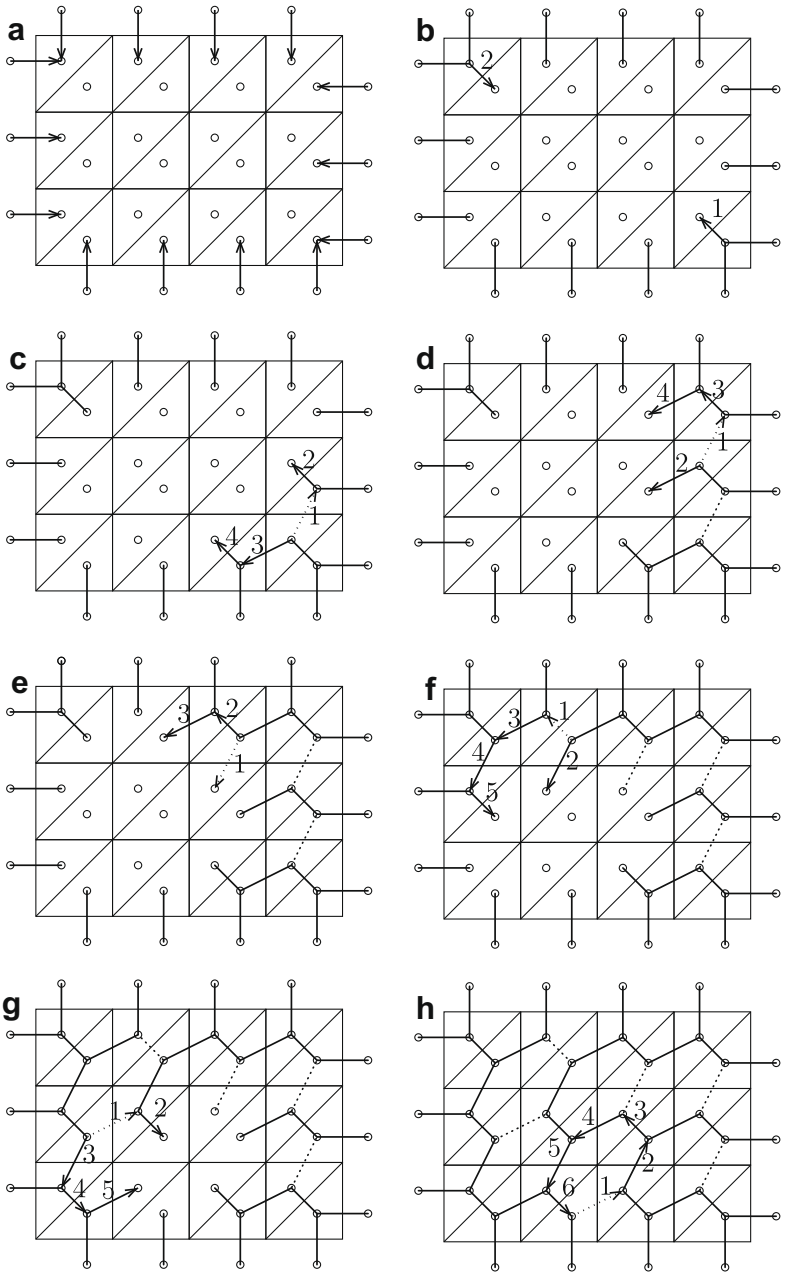

Fig. 11. Grid of size 3×4 with normal velocities 'inherited' from neighbour cells.

Subfigure (a) shows the inheritance from the ghost cells.

If a cell has inherited two velocity components from neighbouring cells, then its velocity vector is fully determined and the cell itself can pass on a normal velocity component to the remaining neighbour. Translated into the graph construction this means: once a vertex in G^* has two edges, we are allowed to draw the missing third edge to the remaining neighbour vertex, as depicted in subfigure (b).

If the process of building G^* stalls, there is a free choice to specify an additional velocity component in a cell with only one fixed velocity component. After this 'intervention' its velocity vector is fully determined and the inheritance starts again. We represent such a choice of a velocity component inside a cell by a dotted line to one of its neighbours. In subfigure c) we first draw the dotted line 1, and than the other lines 2, 3 and 4.

This process can be continued until the entire extended dual graph is complete. Counting the dotted lines will give us the number of velocity components that have been chosen during the construction. It is an upper bound on the number of degrees of freedom. In the 3×4-example shown in Fig. 11 we obtain six degrees of freedom: $f_{3,4} = 6$.

3.4.2. Graph theoretic analysis

Using the construction principle presented above, we can now approach a general derivation for the degrees of freedom for $\mathbf{u}^{(0)}$ inside the grid. Imagine some dotted lines are given right from the start. Let us call them *fixed edges*. In terms of *degrees of freedom* this means that all free velocity components have been set right from the beginning. If the construction does not stall until G^* is complete, there is no need to specify a further velocity component. In this case we call the graph *constructable*. How many fixed edges are at least necessary for such a graph to be constructable? The answer agrees with the degrees of freedom we look for.

Instead of *constructing* the extended dual grid graph, we *delete* it, which ends up as the same: let T be a subgraph of G^* where the edges missing in T represent the *fixed edges* from approach above. If the two vector components in a vertex are determined, we are allowed to delete this vertex. The passing on of a component to the remaining neighbour is symbolised by deleting the corresponding edge. Thus, a vertex of degree 1 has inherited already two components and can be deleted together with the adherent edge. These principles can be summarised in the following rule:

Definition 3. Deletion ruleA vertex has to be deleted if it has degree 1.

We want to know the smallest number of edges missing in T, i.e. we look for some sort of maximal subgraph. The following definition specifies this idea:

Definition 4. We call a subgraph T of G^* deletable, if it can be deleted only by applying the rule of deletion. A subgraph T_n is called maximal deletable, if it contains all vertices of G^* and if any additional edge makes the resulting subgraph T_{n+1} no longer deletable, where the subscript n indicates the number of edges in the graph.

The problem of finding the degrees of freedom for a vector field under the zero-jump constraint can now be rephrased: what is the difference between the number of edges in a *maximal deletable* subgraph $T \subset G^*$ and the extended dual grid graph G^*? The answer can be found with the following lemma.

Lemma 5. *T is a maximal deletable subgraph of an extended dual grid graph G^* if and only if G^* is a spanning tree in G^*.*

Proof. Let us assume, in the first part of the proof, that T is a maximal deletable subgraph of G^*. We have to show, that T is a spanning tree in G^*. Since T is deletable, it does not have cycles. This follows from Definition 4, because a cycle has only vertices of degree $\geqslant 2$ and there is no way to start deleting such a part of T with the deletion rule. However, if a cycle in G^* cannot be deleted, T itself cannot be (completely) deleted. Furthermore, from T being maximal follows that T has to be connected and contains all vertices of G^*. To see this, let us assume T is not connected. Then T has at least two components, which can be connected by at least *one additional edge* without creating a cycle. The resulting subgraph is still deletable, but then the original graph was not maximal. With the same argument all vertices of G^* must be contained in the subgraph T. Otherwise T would consist of several components.

In the second part, let us assume that T is a spanning tree in G^*. We have to show that T is a maximal deletable subgraph of G^*. Every tree has at least one leaf, cf. [10], i.e. a vertex of degree 1, which can be deleted – and the result is again a tree. We can continue deleting leafs until the entire graph is deleted. Therefore, any spanning tree is *deletable*. To see that any spanning tree T is *maximal* deletable consider: if we add a further edge to T out of the complement $G^* \setminus T$, we create a cycle and the resulting graph is no longer deletable. Consequently, any spanning tree T in G^* must be a maximal deletable subgraph of G^*. □

It is now time to harvest the fruits from the trees. The number of velocity components which can be chosen arbitrarily equals the number of edges missing in the maximal deletable subgraph T compared to G^*. This number is a constant for every grid, since a spanning tree in a graph has always the same number of edges, cf. [10]. We therefore have the following theorem:

Theorem 1. *Let $\mathbf{u}$ be a discrete vector field defined in the triangular cells of a grid. Let N_e, N_v be the number of edges and vertices in the corresponding extended dual graph G^* and let N_e^{span} be the number of edges of a spanning tree in G^*. The degrees of freedom for $\mathbf{u}$ under the zero-jump constraint is then given by*

$$\boxed{f = N_e - N_e^{\text{span}} = N_e - N_v + 1.} \tag{3.15}$$

Proof. We summarise the derivation of this theorem: the degrees of freedom is the minimal number of edges which can be omitted in G^*, so that the resulting subgraph T is still deletable. According to Lemma 5 such a maximal subgraph must be a spanning tree in G^*. The differences of edges is a fixed number given by $N_e - N_e^{\text{span}}$, which proves the first part of (3.15). The number of edges N_e^{span} in T is related to the number of vertices N_v of G^* by $N_v = N_e^{\text{span}} + 1$, cf. [10]. This proves the second equality in (3.15). □

This theorem can be applied to a general unstructured grid. We restrict the argument, like the rest of the proof, to triangulations derived from Cartesian grids of size $m \times n$, i.e. with $2mn$ triangular cells. It can be easily shown that the degrees of freedom are then given by

$$\boxed{f_{m,n} = (m-1)(n-1).} \tag{3.16}$$

Two questions remain to be answered: *First of all, are $f_{m,n}$ enough degrees of freedom? To be more precise, is $f_{m,n}$ of the same order of magnitude as the number of velocity components in high speed flow?* In high Mach number flows the number of velocity components that are available for representing a physical velocity field is $4mn$ – two components per triangle – while in low Mach number flow the degrees of freedom are approximately mn. The degrees of freedom are therefore reduced by a factor of four but are of the same order of magnitude $\mathcal{O}_S(mn)$ and, in this sense, it is enough. Recall that the statement is restricted to the leading order velocity $\mathbf{u}^{(0)}$ in low Mach number flow. Higher-order terms of the velocity are not zero-jump constrained and therefore do not face the problem of having to few degrees of freedom.

Secondly, are the components that can be chosen arbitrarily dispersed throughout the grid or can exist large regions with all velocity components fixed by the jump constraint? The extended dual graph has elementary cycles positioned around each internal vertex of the primary grid, while the subgraph T has no cycles at all. Therefore, at least one 'missing edge', i.e. an edge of G^* T, must be in the vicinity of each internal vertex of the primary grid. This states that the arbitrary choices for the velocity components are well dispersed.

4. Conclusion and discussion

We have presented numerical data showing that the classical *first-order* Roe scheme does not suffer from the accuracy problem known for Cartesian or dual grids of a triangulation, if applied on a primary grid with triangular cells. It was shown that the semi-discrete asymptotic equations force the first-order pressure $p^{(1)}$ to be constant in space and the jumps of the normal component of the velocity of leading order $\Delta U^{(0)}$ to vanish. The first constraint is in agreement with the physical pressure field for low Mach numbers; the second constraint leaves enough degrees of freedom (DOF) for a physically correct velocity field.

We will extend the reasoning related to the DOF to other cell geometries, which demonstrates the uniqueness of triangular cells. In [11] Guillard et al. show that at the heart of the accuracy problem is the Riemann problem itself: any jump in the leading order (normal) velocity $U^{(0)}$ leads to a first order pressure $p^{(1)}$ — even in the exact solution. Ergo, a variation in $p^{(1)}$ can be avoided, if the velocity field is such that its normal components $U^{(0)}$ are continuous at cell interfaces. (In fact, for constant $p^{(1)}$, it is sufficient to have a vanishing *second order difference* of $\mathbf{u}^{(0)}$ but I expect a similar loss of DOF). Let us calculate the asymptotic DOF for a grid with n cells, where n is large compared to the number of boundary cells. In 2D n cells have $2n$ velocity components to be specified. Each cell has k edges, leading to $\frac{1}{2}kn$ edges asymptotically and the same number of constraints. Applying these thoughts to triangles and quadrangles, we obtain

$$\begin{aligned} f_{2\text{D}} &\sim 2n - \frac{k}{2}n, \\ f_{\triangle} &\sim 2n - \frac{3}{2}n = \frac{1}{2}n, \\ f_{\square} &\sim 2n - \frac{4}{2}n = 0. \end{aligned}$$

We see that in a triangular mesh $1/4$ of the original DOF are lost in low Mach number flows, which is bearable. For cells with $4, 5$ or more edges there are never enough degrees of freedom to represent a physically correct flow field. This also explains why dual grids of triangulations, used in calculations in [7,12], also lead to the accuracy problem of the Roe scheme.

The reasoning can easily be transferred to 3D:

$$\begin{aligned} f_{3\text{D}} &\sim 3n - \frac{k}{2}n, \\ f_{\triangle} &\sim 3n - \frac{4}{2}n = n, \\ f_{\square} &\sim 3n - \frac{6}{2}n = 0. \end{aligned}$$

With a similar result: only tetrahedra allow enough degrees of freedom.

Higher order schemes are more relevant in practice but were not analysed by the authors yet. First numerical experiments with the *second-order* Roe scheme on unstructured triangular grids with the code *HYDSOL* of IAG Stuttgart lead to completely wrong results. We assume that the reconstruction process prevents the establishment of a continuous normal velocity component introducing the wrong pressure field $p^{(1)}$. Schemes with higher order (> 2) allow a smoother reconstruction which seems to prevent the jumps of the normal velocity component and with it the accuracy problem. DG schemes, for example, are known to produce excellent low Mach number flows, cf. Feistauer [13].

Acknowledgments

I want to thank my PhD thesis advisor Prof. Dr. Georg Bader. Special thanks to Dr. Sabine Roller for supporting my usage of the HYDSOL code and for raising my interest in the field of low Mach number flow. Thanks to Prof. Dr. Rupert Klein and Dr. Friedemann Kemm for the fruitful discussions. For the support in the field of graph theory I want to thank Prof. Dr. Ekkehard Köhler

Appendix A. *A.1. Asymptotic equations of the Roe scheme*

The analysis presented here is closely related to the one by Guillard and Viozat et al. in [7]. The major differences are: The nomenclature was changed from Cartesian to irregular grids with triangular cells. Although it is a semi-discrete analysis, we introduce a time scaling which agrees with an explicit time discretisation: the time steps are $\mathcal{O}_S(M)$ due to the CFL condition. This is reflected in the Strouhal number $\mathrm{Str} = 1/M$, appearing as scaling factor for the time derivatives in the conservation laws. Note that the presented analysis in this article is restricted to the steady flow equations, so that this difference will not be of importance. For nomenclature and index notation we refer to Section 3.

The characteristic variables Δw_i can be written in terms of the local coordinate system at the cell interfaces as:

$$\begin{aligned}
\Delta w_1 &= \frac{1}{2a_{il}}\left(\frac{\Delta_{il}p}{a_{il}} - \rho_{il}\Delta_{il}U\right),\\
\Delta w_2 &= \Delta_{il}\rho - \frac{\Delta_{il}p}{a_{il}^2},\\
\Delta w_3 &= \rho_{il}\Delta_{il}V,\\
\Delta w_4 &= \frac{1}{2a_{il}}\left(\frac{\Delta_{il}p}{a_{il}} + \rho_{il}\Delta_{il}U\right).
\end{aligned}$$

The expressions of the eigenvectors are:

$$\mathbf{r}_1(q_{il}) = \begin{pmatrix} 1 \\ u_{il} - a_{il}(n_x)_{il} \\ v_{il} - a_{il}(n_y)_{il} \\ h_{il} - a_{il}U_{il} \end{pmatrix}, \quad \mathbf{r}_2(q_{il}) = \begin{pmatrix} 1 \\ u_{il} \\ v_{il} \\ \frac{1}{2}(u_{il}^2 + v_{il}^2) \end{pmatrix},$$

$$\mathbf{r}_3(q_{il}) = \begin{pmatrix} 0 \\ -(n_y)_{il} \\ (n_x)_{il} \\ V_{il} \end{pmatrix}, \quad \mathbf{r}_4(q_{il}) = \begin{pmatrix} 1 \\ u_{il} + a_{il}(n_x)_{il} \\ v_{il} + a_{il}(n_y)_{il} \\ h_{il} + a_{il}U_{il} \end{pmatrix}.$$

The local eigenvalues are given by

$$\lambda_1 = U_{il} - a_{il}, \quad \lambda_2 = U_{il}, \quad \lambda_3 = U_{il}, \quad \lambda_4 = U_{il} + a_{il}. \tag{5.17}$$

The Roe scheme in two space dimensions is given by

$$\frac{\mathrm{d}}{\mathrm{d}t}\mathbf{q}_i + \frac{1}{A_i}\sum_{l\in v(i)} \Phi(\mathbf{q}_i, \mathbf{q}_l, \mathbf{n}_{il})\delta_{il} = 0$$

with the Roe flux function

$$\Phi(\mathbf{q}_i, \mathbf{q}_l, bfn_{il}) = \frac{F(\mathbf{q}_i) + F(\mathbf{q}_l)}{2} \cdot bfn_{il} + \frac{1}{2}\sum_{k=1}^{4} \mathbf{r}_k(\mathbf{q}_{il})|\lambda_k(\mathbf{q}_{il})|\Delta w_k(\Delta_{il}\mathbf{q}).$$

The physical flux F consists of two space components $F = (\mathbf{f}, \mathbf{g})^T$, cf. Eq. (3.1). For later use, we give the complete system of equations for the transport of mass density ρ, momentum density ρu and ρv, and the density of total energy ρe:

$$A_i \frac{\mathrm{d}}{\mathrm{d}t}\rho_i + \frac{1}{2}\sum_{l\in\nu(i)} \rho_l \mathbf{u}_l \cdot \mathbf{n}_{il}\delta_{il} + \frac{1}{2}\sum_{l\in\nu(i)} \left\{ |U_{il}|(\Delta_{il}\rho - \frac{\Delta_{il}p}{a_{il}^2}) + \rho_{il}\frac{U_{il}}{a_{il}}\Delta_{il}U + \frac{\Delta_{il}p}{a_{il}} \right\}\delta_{il} = 0, \tag{5.18}$$

$$A_i \frac{\mathrm{d}}{\mathrm{d}t}\rho_i u_i + \frac{1}{2}\sum_{l\in\nu(i)} \{\rho_l u_l \mathbf{u}_l \cdot \mathbf{n}_{il} + p_l (n_x)_{il}\}\delta_{il} + \frac{1}{2}\sum_{l\in\nu(i)} \left\{ |U_{il}|(\Delta_{il}\rho - \frac{\Delta_{il}p}{a_{il}^2})u_{il} + \rho_{il}\frac{U_{il}}{a_{il}}u_{il}\Delta_{il}U \right\}\delta_{il}$$
$$+ \frac{1}{2}\sum_{l\in\nu(i)} \left\{ -\rho_{il}|U_{il}|(n_y)_{il}\Delta_{il}V + \frac{(Un_x + u)_{il}}{a_{il}}\Delta_{il}p + \rho_{il}a_{il}(n_x)_{il}\Delta_{il}U \right\}\delta_{il} = 0, \tag{5.19}$$

$$A_i \frac{\mathrm{d}}{\mathrm{d}t}\rho_i v_i + \frac{1}{2}\sum_{l\in\nu(i)} \{\rho_l v_l \mathbf{u}_l \cdot \mathbf{n}_{il} + p_l (n_x)_{il}\}\delta_{il} + \frac{1}{2}\sum_{l\in\nu(i)} \left\{ |U_{il}|(\Delta_{il}\rho - \frac{\Delta_{il}p}{a_{il}^2})v_{il} + \rho_{il}\frac{U_{il}}{a_{il}}v_{il}\Delta_{il}U \right\}\delta_{il}$$
$$+ \frac{1}{2}\sum_{l\in\nu(i)} \left\{ \rho_{il}|U_{il}|(n_x)_{il}\Delta_{il}V + \frac{(Un_y + v)_{il}}{a_{il}}\Delta_{il}p + \rho_{il}a_{il}(n_y)_{il}\Delta_{il}U \right\}\delta_{il} = 0, \tag{5.20}$$

$$A_i \frac{\mathrm{d}}{\mathrm{d}t}\rho_i e_i + \frac{1}{2}\sum_{l\in\nu(i)} (\rho_l e_l + p_l)\mathbf{u}_l \cdot \mathbf{n}_{il}\delta_{il} + \frac{1}{2}\sum_{l\in\nu(i)} \left\{ |U_{il}|(\Delta_{il}\rho - \frac{\Delta_{il}p}{a_{il}^2})\frac{u_{il}^2 + v_{il}^2}{2} + \rho_{il}\frac{U_{il}}{a_{il}}h_{il}\Delta_{il}U \right\}\delta_{il}$$
$$+ \frac{1}{2}\sum_{l\in\nu(i)} \left\{ \rho_{il}|U_{il}|V_{il}\Delta_{il}V + \frac{(h + U^2)_{il}}{a_{il}}\Delta_{il}p + \rho_{il}a_{il}U_{il}\Delta_{il}U \right\}\delta_{il} = 0. \tag{5.21}$$

A.1.1. Nondimensionalisation

We introduce the following scalings: l_{ref} is the reference length, p_{ref} is the reference pressure, ρ_{ref} is the reference density, $a_{\mathrm{ref}}^2 = p_{\mathrm{ref}}/\rho_{\mathrm{ref}}$ is the reference speed of sound, u_{ref} is the reference flow velocity, $t_{\mathrm{ref}} = l_{\mathrm{ref}}/a_{\mathrm{ref}}$ is the reference time and $h_{\mathrm{ref}} = \frac{p_{\mathrm{ref}}}{\rho_{\mathrm{ref}}} = a_{\mathrm{ref}}^2$ is the reference specific total enthalpy. The dimensionless numbers relevant to this type of flow are Mach and Strouhal number:

$$\mathrm{M} = \frac{u_{\mathrm{ref}}}{a_{\mathrm{ref}}} \quad \text{and} \quad \mathrm{Str} = \frac{l_{\mathrm{ref}}/t_{\mathrm{ref}}}{u_{\mathrm{ref}}} = \frac{1}{\mathrm{M}}.$$

In the following, all equations are sorted by orders of magnitude in M. The nondimensional form of the *continuity equation* is

$$\mathrm{M}^0 A_i \frac{\mathrm{d}}{\mathrm{d}t}\rho_i + \frac{1}{2}\sum_{l\in\nu(i)} \frac{\Delta_{il}p}{a_{il}}\delta_{il} + \mathrm{M}^1 \frac{1}{2}\sum_{l\in\nu(i)} \left\{ \rho_l \mathbf{u}_l \cdot \mathbf{n}_{il} + |U_{il}|(\Delta_{il}\rho - \frac{\Delta_{il}p}{a_{il}^2}) \right\}\delta_{il} + \mathrm{M}^2 \frac{1}{2}\sum_{l\in\nu(i)} \rho_{il}\frac{U_{il}}{a_{il}}\Delta_{il}U\delta_{il} = 0. \tag{C}$$

A similar procedure leads to the *equation of x-momentum conservation*:

$$\mathrm{M}^{-1}\frac{1}{2}\sum_{l\in\nu(i)} p_l (n_x)_{il}\delta_{il} + \mathrm{M}^0 A_i \frac{\mathrm{d}}{\mathrm{d}t}\rho_i u_i + \frac{1}{2}\sum_{l\in\nu(i)} \left\{ \frac{(Un_x + u)_{il}}{a_{il}}\Delta_{il}p + \rho_{il}a_{il}(n_x)_{il}\Delta_{il}U \right\}\delta_{il}$$
$$+ \mathrm{M}^1 \frac{1}{2}\sum_{l\in\nu(i)} \left\{ \rho_l u_l \mathbf{u}_l \cdot \mathbf{n}_{il} + |U_{il}|(\Delta_{il}\rho - \frac{\Delta_{il}p}{a_{il}^2})u_{il} - \rho_{il}|U_{il}|(n_y)_{il}\Delta_{il}V \right\}\delta_{il} + \mathrm{M}^2 \frac{1}{2}\sum_{l\in\nu(i)} \rho_{il}\frac{U_{il}}{a_{il}}u_{il}\Delta_{il}U\delta_{il} = 0, \tag{$\mathrm{M_x}$}$$

and the *equation of y-momentum conservation*:

$$\mathrm{M}^{-1}\frac{1}{2}\sum_{l\in\nu(i)} p_l (n_y)_{il}\delta_{il} + \mathrm{M}^0 A_i \frac{\mathrm{d}}{\mathrm{d}t}\rho_i v_i + \frac{1}{2}\sum_{l\in\nu(i)} \left\{ \frac{(Un_y + v)_{il}}{a_{il}}\Delta_{il}p + \rho_{il}a_{il}(n_y)_{il}\Delta_{il}U \right\}\delta_{il}$$
$$+ \mathrm{M}^1 \frac{1}{2}\sum_{l\in\nu(i)} \left\{ \rho_l v_l \mathbf{u}_l \cdot \mathbf{n}_{il} + |U_{il}|(\Delta_{il}\rho - \frac{\Delta_{il}p}{a_{il}^2})v_{il} - \rho_{il}|U_{il}|(n_x)_{il}\Delta_{il}V \right\}\delta_{il} + \mathrm{M}^2 \frac{1}{2}\sum_{l\in\nu(i)} \rho_{il}\frac{U_{il}}{a_{il}}v_{il}\Delta_{il}U\delta_{il} = 0. \tag{$\mathrm{M_y}$}$$

The *equation of energy conservation* in non-dimensional form is

$$\mathrm{M}^{-1}\frac{1}{2}\sum_{l\in\nu(i)} \left\{ |U_{il}|(\Delta_{il}\rho - \frac{\Delta_{il}p}{a_{il}^2})\frac{u_{il}^2 + v_{il}^2}{2} + \rho_{il}|U_{il}|V_{il}\Delta_{il}V \right\}\delta_{il} + \mathrm{M}^0 A_i \frac{\mathrm{d}}{\mathrm{d}t}\rho_i e_i + \frac{1}{2}\sum_{l\in\nu(i)} \frac{h_{il}}{a_{il}}\Delta_{il}p\delta_{il}$$
$$+ \mathrm{M}^1 \frac{1}{2}\sum_{l\in\nu(i)} (\rho_l e_l + p_l)\mathbf{u}_l \cdot \mathbf{n}_{il}\delta_{il} + \mathrm{M}^2 \frac{1}{2}\sum_{l\in\nu(i)} \left\{ \frac{U_{il}^2}{a_{il}}\Delta_{il}p + \rho_{il}a_{il}U_{il}\Delta_{il}U + \rho_{il}\frac{U_{il}}{a_{il}}h_{il}\Delta_{il}U \right\}\delta_{il} = 0. \tag{E}$$

A.1.2. Asymptotic equations

As in the continuous asymptotic analysis, we assume for all physical quantities ϕ an asymptotic 3-term expansion

$$\phi = \phi^{(0)} + \mathrm{M}\phi^{(1)} + \mathrm{M}^2\phi^{(2)} + calO(\ \mathrm{M}^2) \quad \text{as } \mathrm{M} \to 0$$

and insert these expansions in the semi-discrete equations. They read, sorted by powers of the Mach number:

Order M^{-1}*:*

$$\sum_{l\in v(i)} p_l^{(0)}(n_x)_{il}\delta_{il} = 0, \tag{M_x^{-1}}$$

$$\sum_{l\in v(i)} p_l^{(0)}(n_y)_{il}\delta_{il} = 0. \tag{M_y^{-1}}$$

Order M^0*:*

$$A_i \frac{d}{dt}\rho_i^{(0)} + \frac{1}{2}\sum_{l\in v(i)} \frac{\Delta_{il}p^{(0)}}{a_{il}^{(0)}}\delta_{il} = 0, \tag{C_0}$$

$$A_i \frac{d}{dt}\rho_i^{(0)}u_i^{(0)} + \frac{1}{2}\sum_{l\in v(i)} p_l^{(1)}(n_x)_{il}\delta_{il} + \frac{1}{2}\sum_{l\in v(i)} \left\{ \frac{(U^{(0)}n_x + u^{(0)})_{il}}{a_{il}^{(0)}}\Delta_{il}p^{(0)} + \rho_{il}^{(0)}a_{il}^{(0)}(n_x)_{il}\Delta_{il}U^{(0)} \right\}\delta_{il} = 0, \tag{M_x^0}$$

$$A_i \frac{d}{dt}\rho_i^{(0)}v_i^{(0)} + \frac{1}{2}\sum_{l\in v(i)} p_l^{(1)}(n_y)_{il}\delta_{il} + \frac{1}{2}\sum_{l\in v(i)} \left\{ \frac{(U^{(0)}n_y + v^{(0)})_{il}}{a_{il}^{(0)}}\Delta_{il}p^{(0)} + \rho_{il}^{(0)}a_{il}^{(0)}(n_y)_{il}\Delta_{il}U^{(0)} \right\}\delta_{il} = 0, \tag{M_y^0}$$

$$A_i \frac{d}{dt}\rho_i^{(0)}e_i^{(0)} + \frac{1}{2}\sum_{l\in v(i)} \frac{h_{il}^{(0)}}{a_{il}^{(0)}}\Delta_{il}p^{(0)}\delta_{il} = 0. \tag{E_0}$$

Order M^1*:*

$$A_i \frac{d}{dt}\rho_i^{(1)} + \frac{1}{2}\sum_{l\in v(i)} \left\{ \frac{\Delta_{il}p^{(1)}}{a_{il}^{(0)}} + \rho_l^{(0)}\mathbf{u}_l^{(0)}\cdot\mathbf{n}_{il} + |U_{il}^{(0)}|\left(\Delta_{il}\rho^{(0)} - \frac{\Delta_{il}p^{(0)}}{(a_{il}^{(0)})^2}\right) \right\}\delta_{il} = 0, \tag{C_1}$$

$$\begin{aligned} A_i \frac{d}{dt}(\rho_i u_i)^{(1)} &+ \frac{1}{2}\sum_{l\in v(i)} p_l^{(2)}(n_x)_{il}\delta_{il} + \frac{1}{2}\sum_{l\in v(i)} \left\{ \frac{[(Un_x + u)_{il}\Delta_{il}p]^{(1)}}{a_{il}^{(0)}} + [\rho_{il}a_{il}(n_x)_{il}\Delta_{il}U]^{(1)} \right. \\ &\left. + \rho_l^{(0)}u_l^{(0)}\mathbf{u}_l^{(0)}\cdot\mathbf{n}_{il} + |U_{il}^{(0)}|\left(\Delta_{il}\rho^{(0)} - \frac{\Delta_{il}p^{(0)}}{(a_{il}^{(0)})^2}\right)u_{il}^{(0)} - \rho_{il}^{(0)}|U_{il}^{(0)}|(n_y)_{il}\Delta_{il}V^{(0)} \right\}\delta_{il} = 0, \end{aligned} \tag{M_x^1}$$

$$\begin{aligned} A_i \frac{d}{dt}(\rho_i v_i)^{(1)} &+ \frac{1}{2}\sum_{l\in v(i)} p_l^{(2)}(n_y)_{il}\delta_{il} + \frac{1}{2}\sum_{l\in v(i)} \left\{ \frac{[(Un_y + v)_{il}\Delta_{il}p]^{(1)}}{a_{il}^{(0)}} + [\rho_{il}a_{il}(n_y)_{il}\Delta_{il}U]^{(1)} \right. \\ &\left. + \rho_l^{(0)}v_l^{(0)}\mathbf{u}_l^{(0)}\cdot\mathbf{n}_{il} + |U_{il}^{(0)}|\left(\Delta_{il}\rho^{(0)} - \frac{\Delta_{il}p^{(0)}}{(a_{il}^{(0)})^2}\right)v_{il}^{(0)} + \rho_{il}^{(0)}|U_{il}^{(0)}|(n_x)_{il}\Delta_{il}V^{(0)} \right\}\delta_{il} = 0, \end{aligned} \tag{M_y^1}$$

$$A_i \frac{d}{dt}(\rho_i e_i)^{(1)} + \frac{1}{2}\sum_{l\in v(i)} \left\{ \frac{(h_{il}\Delta_{il}p)^{(1)}}{a_{il}^{(0)}} + (\rho_l^{(0)}e_l^{(0)} + p_l^{(0)})\mathbf{u}_l^{(0)}\cdot\mathbf{n}_{il} \right\}\delta_{il} = 0. \tag{E_1}$$

The terms in brackets with a superscript can be expanded using the rules for asymptotic expressions [12]. The equations corresponding to the order M^2 are not needed for the presented analysis. In the following we extract the equations for pressure and velocity from the equations of mass, momentum and energy.

Evolution equation for $\mathbf{p}^{(0)}$ To find the evolution equation for the pressure of leading order we replace in (E_0) the energy density $(\rho e)^{(0)}$ by $p^{(0)}/(\gamma-1)$ using the perfect gas law of leading order and obtain

$$\frac{d}{dt}p^{(0)} + \frac{\gamma-1}{2}\frac{1}{A_i}\sum_{l\in v(i)} \frac{h_{il}^{(0)}}{a_{il}^{(0)}}\Delta_{il}p^{(0)}\delta_{il} = 0 \tag{P_0}$$

Semi-discrete equation for $\mathbf{p}^{(1)}$ and $\mathbf{u}^{(0)}$ To find the *evolution equation for* $p^{(1)}$ we replace the energy density $(\rho e)^{(1)}$ in Eq. (E_1) by the pressure $p^{(1)}$

$$(\rho_i e_i)^{(1)} = \varepsilon_i^{(1)} = \frac{1}{\gamma-1}p_i^{(1)}.$$

We use the fact $p^{(0)} = \text{const}$, proved in Section 3.2, which implies $h^{(0)} = \text{const}$. This simplifies the Roe averages to $h_{il}^{(0)} = h_i^{(0)}$ and $a_{il}^{(0)} = a_i^{(0)}$. Using

$$h_i^{(0)} = \frac{\gamma}{\gamma-1}\frac{p_i^{(0)}}{\rho_i^{(0)}} \quad \text{and} \quad (a_i^{(0)})^2 = \frac{\gamma p_i^{(0)}}{\rho_i^{(0)}},$$

the second term of (E_1) can further be transformed to

$$\frac{(h_{il}\Delta_{il}p)^{(1)}}{a_{il}^{(0)}} = \frac{h_{il}^{(0)}\Delta_{il}p^{(1)} + h_{il}^{(1)}\Delta_{il}p^{(0)}}{a_{il}^{(0)}} = \frac{a_i^{(0)}}{\gamma - 1}\Delta_{il}p^{(1)}.$$

In the third term we use

$$(\rho_l^{(0)}e_l^{(0)} + p_l^{(0)}) = \frac{\gamma}{\gamma - 1}p_l^{(0)}$$

and obtain the

Evolution equation for $\mathbf{p}^{(1)}$*:*

$$\underbrace{\frac{\mathrm{d}}{\mathrm{d}t}p_i^{(1)}}_{\frac{\partial}{\partial t}p^{(1)}} + \underbrace{\gamma p_i^{(0)}\frac{1}{A_i}\sum\nolimits_{l\in v(i)}\frac{\mathbf{u}_l^{(0)}\cdot\mathbf{n}_{il}}{2}\delta_{il}}_{\gamma p^{(0)}\nabla\cdot\mathbf{u}^{(0)}} = \underbrace{-\frac{1}{2}a_i^{(0)}\frac{1}{A_i}\sum\nolimits_{l\in v(i)}\Delta_{il}p^{(1)}\delta_{il}}_{\frac{1}{2}a^{(0)}\nabla^2 p^{(1)}\delta}. \qquad (P_1)$$

The underbracing shows the terms appearing in the corresponding modified equation. The second term in (P_1) is the numerical viscosity of the scheme and is $\mathcal{O}(\delta)$ as it should be for a first-order scheme.

We do a similar transformation of (M_x^0) to derive the equation for $\mathbf{u}^{(0)}$. Omitting $\Delta_{il}p^{(0)}$ and replacing the Roe averages of constant quantities by their node values $\rho_{il}^{(0)} = \rho_i^{(0)}$ and $a_{il}^{(0)} = a_i^{(0)}$, we obtain the

Evolution equation for $\mathbf{u}^{(0)}$*:*

$$\underbrace{\frac{\mathrm{d}}{\mathrm{d}t}u_i^{(0)}}_{\frac{\partial}{\partial t}u^{(0)}} + \underbrace{\frac{1}{\rho_i^{(0)}}\frac{1}{A_i}\sum\nolimits_{l\in v(i)}\frac{p_l^{(1)}(n_x)_{il}}{2}\delta_{il}}_{\frac{1}{\rho^{(0)}}\frac{\partial}{\partial x}p^{(1)}} = \underbrace{-\frac{1}{2}\frac{a_i^{(0)}}{\rho_i^{(0)}}\frac{1}{A_i}\sum\nolimits_{l\in v(i)}\rho_{il}^{(0)}\Delta_{il}U^{(0)}(n_x)_{il}\delta_{il}}_{\frac{1}{2}a^{(0)}\frac{\partial^2}{\partial x^2}u^{(0)}\delta}. \qquad (U_0)$$

Beneath the equations, the corresponding continuous terms are given. For completeness we also give the

Evolution equation for $\mathbf{v}^{(0)}$*:*

$$\underbrace{\frac{\mathrm{d}}{\mathrm{d}t}v_i^{(0)}}_{\frac{\partial}{\partial t}v^{(0)}} + \underbrace{\frac{1}{\rho_i^{(0)}}\frac{1}{A_i}\sum\nolimits_{l\in v(i)}\frac{p_l^{(1)}(n_y)_{il}}{2}\delta_{il}}_{\frac{1}{\rho^{(0)}}\frac{\partial}{\partial y}p^{(1)}} = \underbrace{-\frac{1}{2}\frac{a_i^{(0)}}{\rho_i^{(0)}}\frac{1}{A_i}\sum\nolimits_{l\in v(i)}\rho_{il}^{(0)}\Delta_{il}U^{(0)}(n_y)_{il}\delta_{il}}_{\frac{1}{2}a^{(0)}\frac{\partial^2}{\partial y^2}v^{(0)}\delta}. \qquad (V_0)$$

References

[1] R.J. Leveque, Finite Volume Methods for Hyperbolic Problems Cambridge Texts in Applied Mathematics, Cambridge University Press, Cambridge, 2002.
[2] J. Sesterhenn, B. Müller, H. Thomann, On the cancellation problem in calculating compressible low Mach number flows, J. Comput. Phys. 151 (2) (1999) 597–615.
[3] E. Turkel, Preconditioned methods for solving the incompressible and low speed compressible equations, J. Comput. Phys. 72 (1987) 277–298.
[4] E. Turkel, A. Fiterman, B. van Leer, Preconditioning and the limit of the compressible to the incompressible flow equations for finite difference schemes, Frontiers of Computational Fluid Dynamics 1994, CMAS: Computational Methods in Applied Sciences, Chichester: Wiley, 1995
[5] B. van Leer, W.-T. Lee, P. Roe, Characteristic time-stepping or local preconditioning of the euler equations, AIAA paper 91-1552, 1991.
[6] Y.-H. Choi, C. Merkle, The application of preconditioning in viscous flows, J. Comput. Phys. 105 (2) (1993) 207–223.
[7] H. Guillard, C. Viozat, On the behaviour of upwind schemes in the low Mach number limit, Comput. Fluids 28 (1) (1999) 63–86.
[8] F. Rieper, On the behaviour of numerical schemes in the low Mach number regime, Ph.D. thesis, Brandenburg Technical University, Cottbus, 2008.
[9] R. Klein, Semi-implicit extension of a Godunov-type scheme based on low Mach number asymptotics I: one-dimensional flow, J. Comput. Phys. 121 (2) (1995) 213–237.
[10] D.B. West, Introduction to Graph Theory, second ed., Prentice-Hall of India, New Delhi, 2005.
[11] H. Guillard, A. Murrone, On the behavior of upwind schemes in the low Mach number limit. II: Godunov type schemes, Comput. Fluids 33 (4) (2004) 655–675.
[12] A. Meister, Analyse und Anwendung Asymptotik-basierter numerischer Verfahren zur Simulation reibungsbehafteter Strömungen in allen Mach-Zahlbereichen, Habilitationsschrift, Universität Hamburg, 2001.
[13] M. Feistauer, V. Kucera, On a robust discontinuous Galerkin technique for the solution of compressible flow, J. Comput. Phys. 224 (1) (2007) 208–221.